Title	Development of low-cost multi-wavelength imager system for studies of aurora and airglow
Authors	Ogawa Y., Tanaka Y., Kadokura A., Hosokawa K., Ebihara Y., Motoba T., Gustavsson B., Brändström U., Sato Y., Oyama S., Ozaki M., Raita T., Sigernes F., Nozawa S., Shiokawa K., Kosch M., Kauristie K., Hall C., Suzuki S., Miyoshi Y., Gerrard A., Miyaoka H., and Fujii R.
Citation	Polar Science（Available online 16 December 2019.）
Issue Date	To be issued in 2020
Type	Journal Article
URL	https://doi.org/10.1016/j.polar.2019.100501
Right	CC BY 4.0
Textversion	preprint

Development of low-cost multi-wavelength imager system for studies of auroras and airglows

Ogawa, Y.[1,2,3], Y. Tanaka[1,2,3], A. Kadokura[1,2,3], K. Hosokawa[4], Y. Ebihara[5], T. Motoba[6], B. Gustavsson[7], U. Brändström[8], Y. Sato[9], S. Oyama[10,11], T. Raita[12], F. Sigernes[13], S. Nozawa[10], K. Shiokawa[10], M. Kosch[14,15], K. Kauristie[16], C. Hall[7], S. Suzuki[17], Y. Miyoshi[10], A. Gerrard[18], H. Miyaoka[1], and R. Fujii[19]

[1] National Institute of Polar Research, Japan

[2] The Graduate University for Advanced Studies (SOKENDAI), Japan

[3] Joint Support-Center for Data Science Research, Research Organization of Information and Systems, Japan

[4] Graduate School of Informatics and Engineering, The University of Electro-Communications, Japan

[5] Research Institute for Sustainable Humanosphere, Kyoto University, Japan

[6] The Johns Hopkins University Applied Physics Laboratory, USA

[7] UiT The Arctic University of Norway, Norway

[8] Swedish Institute of Space Physics, Sweden

[9] Nippon institute of technology, Tokyo, Japan

[10] Institute for Space–Earth Environmental Research, Nagoya University, Japan

[11] University of Oulu, Finland

[12] Sodankylä Geophysical Observatory, Finland

[13] University Centre in Svalbard, Norway

[14] South African National Space Agency, South Africa

[15] Lancaster University, UK

[16] Finnish Meteorological Institute, Finland

[17] Aichi University, Japan

[18] Center for Solar-Terrestrial Research, New Jersey Institute of Technology, USA.

[19] Research Organization of Information and Systems, Japan

Corresponding author: Yasunobu Ogawa (yogawa@nipr.ac.jp)

Abstract (less than 200 words)

This paper introduces a new system that can monitor auroras and atmospheric airglows using a low-cost Watec monochromatic imager (WMI) equipped with a sensitive camera, a filter with high transmittance, and the optics which do not make parallel ray paths. The WMI system with 486-nm, 558-nm, and 630-nm band-pass filters has observable luminosity of about ~200 – 4000 Rayleigh for 1.07-sec exposure time and about ~40 – 1200 Rayleigh for 4.27-sec exposure time, for example. It is demonstrated that the WMI system is capable of detecting 428-nm auroral intensities properly, through comparison with those measured with a collocated electron-multiplying charge-coupled device (EMCCD) imager system with narrower band-pass filter. The WMI system has two distinct advantages over the existing system: One makes it possible to reduce overall costs, and the other is that it enables the continuous observation even under twilight and moonlight conditions. Since 2013 a set of multi-wavelength WMIs has been operating in northern Scandinavia, Svalbard, and Antarctica to study meso- and large-scale aurora and airglow phenomena. Future development of the low-cost WMI system is expected to provide a great opportunity for constructing a global network for multi-wavelength aurora and airglow monitoring.

Keywords: aurora, airglow, imager, polar ionosphere

1. Introduction

Due to the rapid development of cameras and computers in recent years, various progress and new directions are seen in aurora and airglow observations. For example, electron-multiplying charge-coupled device (EMCCD) cameras and/or Scientific CMOS (sCMOS) cameras are used for ultra-sensitive high-speed aurora observations [e.g., Kataoka et al., 2011; Ozaki et al., 2018], and panchromatic observations (time resolution of about 4-sec) by

55 the all-sky panchromatic camera network have been carried out by the THEMIS Ground Based Observatory
56 (GBO) [e.g., Donovan et al., 2006]. However, it is difficult to discuss the average energy and flux of precipitating
57 electrons quantitatively from observations with the all-sky panchromatic camera network. Also, it is still difficult
58 to develop an observation network using high-specification cameras or monochrome optical systems due to their
59 high costs. Optical instruments with filter wheels have been used for observations of multiple wavelengths. They
60 require mechanical motion, and the temporal resolution of each wavelength is limited to several seconds or longer.
61
62 In this paper, we introduce an observation system which solves some of the problems mentioned above. The
63 observation system, named Watec Monochromatic Imager (WMI), consists of a highly-sensitive camera made by
64 Watec Co. ltd, a fast lens by Fujinon Co. ltd, a band-pass filter with high transmittance, and is characterized by an
65 optical system that does not produce parallel light. Cost of the WMI system is about one-hundredth of
66 monochrome EMCCD/sCMOS imager systems, but the system has enough sensitivity for the study of
67 aurora/airglow. The low-cost system therefore enables us to make multi-wavelength and multipoint aurora/airglow
68 observations. We have extended observations of the multi-wavelength WMI imagers in northern Scandinavia,
69 Svalbard, and Antarctica since 2013.
70
71 The WMI system composes of simple and high-transmittance optics with a fisheye lens and an optical filter with
72 high transmittance. The system allows us to obtain images with the time resolution of about 1 sec, and therefore
73 auroral substorms [e.g., Akasofu, 1964] with high spatiotemporal variations and pulsating aurora with a period of
74 about several seconds can be targets to study with the WMI system. Other advances of the WMI system are that
75 (1) maintenance of the WMI system (e.g., replacement of cameras, lenses and filters) is easy, and (2) the WMI
76 system enables the continuous observation even under twilight and moonlight conditions because the risk of the
77 WMI camera damage due to twilight or moonlight is relatively low. Disadvantages of this WMI system are that
78 (1) the resolution of the WMI camera data is 8 bits (256 gradations) whereas expensive cameras are usually 16
79 bits (65,536 gradations), (2) contamination of several aurora and airglow emissions near the typical auroral
80 emissions for WMI (428-nm, 558-nm, and 630-nm) has to be taken into account because the WMI system utilzes
81 band-pass filters with a bandwidth of 10 nm, and (3) the WMI system does not utilize a cooled CCD, and the data

from the camera is an analog video signal so that its noise level is relatively high.

When regular observations are performed with the multi-wavelength WMI system at multiple points, a huge amount of data are accumulated. One image of the system has typically 200 k bytes, and a total amount of their data size is about 8 M bytes per second at the current nine stations. A total of approximately 50 T bytes of disk capacity is required in one year. We have also developed a storage and web server system that integrate and maintain the large amounts of WMI data. In this paper, we explain the outline of the low-cost multi-wavelength WMI observation system and discuss the possibilities and the future development based on data/results obtained using the system.

2. A multi-wavelength WMI imager system

Figure 1 shows examples of multi-wavelength WMI cameras in Tromsø, Norway and Longyearbyen, Svalbard. Eight cameras are installed and operated in each optical dome with a diameter of approximately 1-m. In addition to the WMI all-sky cameras, narrow field of view (FOV) and/or wide FOV camera(s) are included.

Figure 2 shows an overview of data flows of (a) the WMI observation system in polar regions and (b) the data processing system in the National Institute of Polar Research (NIPR). Analog video signals coming out of the WMI cameras are converted into digital images (with a jpeg format) by a video encoder, and then the images are stored in two PCs in the beginning. The image data are compiled as a tar file every hour and stored in Network Attached Storage (NAS) next. The data are regularly downloaded to NIPR using another PC for data transfer. This data transfer is divided into two types: Transfer of real-time data open to the public (including keogram created automatically at the observation sites) and data transfer of raw images. When transferring raw data, a considerable load on the network occurs, and it causes failure of transferring and storing real-time images. To avoid the problem, we constructed two separated network groups in the WMI system using two routers and NAS with two network ports: (i) A network group for real-time data acquisition from the video encoder to the PCs and (ii) a network

group for subsequent data transfer to outside.

The optical data transferred to NIPR has been stored in multiple NAS, and secondary processing is performed using several workstations. Some of the jpeg image files have been converted to CDF data format files, in collaboration with IUGONET project [e.g., Hayashi et al., 2013; Tanaka et al., 2013]. The IUGONET developed an integrated analysis system in collaboration with the SPEDAS project [Angelopoulos et al., 2018]. Most of the WMI databases are open to the public via a web page (http://pc115.seg20.nipr.ac.jp/www/opt/index.html).

Table 1 shows the individual device names used in the WMI system and their specifications. The WAT-910 HX camera made by Watec Co. has been used for the system since 2013. The camera has four times higher sensitivity than the previous camera (WAT-120 N+ made by Watec Co.) which had been used before 2013. Also, color cameras named WAT-233 and WAT-221S2 have been used to distinguish clouds and auroras. Fujinon's fisheye lens (F1.4) has been used, and also wide/narrow FOV observations are simultaneously used. For the three colors (428-nm, 558-nm, and 630-nm), a band-pass filter having the full width at half maximum (FWHM) of 10 nm is used. In addition, a wider band-pass filter with FWHM of 50 nm for auroras at a wavelength of ~670-nm is also used. The top part of the Watec camera is cut to insert the bandpass filter between the lens and CCD surface of the camera. The video encoders, AXIS Q7404, enables us to transfer a large amount of data from multiple cameras to PCs via Gigabit Ethernet cables.

3. Calibration of filters and sensitivities of the WMI system

For monochrome aurora/airglow imagers such as ASI-1 and ASI-2 [Taguchi et al., 2004], an optical system with a parallel ray path has been designed. The parallel ray path is created by combining numerous lenses, and consequently its transmittance is reduced (about 50 – 70%, private communication with Dr. Taguchi). Then, a narrow band-pass interference filter (FWHM: 1.5 ~ 3.0 nm) with transmittance of typically about 40 – 50% has been used for the monochrome imagers. On the other hand, this WMI system does not produce parallel ray path to prevent a decrease in transmittance, and therefore the light passes the filter obliquely (see Figure 1c). The all-

sky image projected on to the image plane has a diameter of 4.5mm which fits within the CCD chip size of 6.0 mm × 7.4 mm. Since the distance between the CCD surface and the eyepiece lens is about 9 mm, the incident angles of the ray path are mostly within about 18 deg (= $\tan^{-1}(3/9)$). Based on the condition of the incident angle when inserting a filter between the eyepiece and the CCD surface, we examined the capability of the aurora emission observations using the WMI system.

Figure 3 shows the angular dependence of the transmission characteristics of the three filters used for typical auroral emissions (428-nm, 558-nm, and 630-nm) measured with the U-3300 spectrophotometer made by Hitachi High-Tech Science Corporation. As the incident angle increases, the transmission region shifts to the shorter wavelength, while the shape of the transmittance band does not change significantly. Their transmittance is still high (80 – 95%). The stable transmittance of the filters to the incident angle is important when we derive absolute values of auroral emission intensities. When the angle exceeds 20 degrees, auroral emissions are outside the passband. Thus we confirmed that the imager system should work if the incident angle to the filter is within ~18 degrees. Regarding the filter for 630-nm aurora/airglow emission, it was found that the aurora emission of 636.4-nm is also included slightly when the incident angle is small. The shift of the transmission region λ_θ can be theoretically described using the following equation.

$$\lambda_\theta = \lambda_0 (1 - (Ne / N^*)^2 \sin^2\theta)^{1/2}$$
$$\sim \lambda_0 (1 - \theta^2 / 2 N^{*2}), \quad (1)$$

where θ is the incident angle, λ_0 is the wavelength when the incident angle θ equals to zero, Ne is the refractive index of outside media (equal to 1.0), and N^* is the refractive index of the filter (typically ~2.05 for band-pass filters by Andover Co.). The theoretical shift values of the center wavelengths are marked by blue symbols in the bottom of each plot in Figure 3. We found that the theoretical shifts are in good agreement with the observed shifts.

The sensitivity of the WMI system has been calibrated against a National Institute of Standards and Technology (NIST) traceable 1.9-m integration sphere (Labsphere LMS-760) at NIPR. Figure 4a shows a sample image of the

integration sphere taken using the WMI imager with 558-nm band-pass filter and a 1-sec exposure time. It is found that the sensitivity is almost circularly symmetric. The background count level is already subtracted by using a dark image. The original image has a high count area on the upper left of the image, which is considered to be a characteristic of the CCD image sensor (Sony ICX2428ALL, interline system) of the camera. These calibration data serve as correction factors for sensitivity field flatness. The optics of the WMI system exhibit moderate vignetting, similar to the ASI-2 (Taguchi et al., 2004). Sensitivity at the horizon (~230 pixels from the zenith) is about two thirds of the peak sensitivity at the zenith (see Figure 4b). The ratio of sensitivity at a certain distance from the zenith to that at the zenith was approximated using the following equation.

$$\mathrm{Count}(R) / \mathrm{Count}(R=0) = \alpha \times R^2 + 1 \quad (2)$$

where R indicates radial distance (in pixel). α was estimated to be $\sim 6.3 \times 10^{-6}$, using many samples with several filters and luminosity. The ratio is used to calculate sensitivity field flatness, and one of the results is shown in Figure 4c.

Figure 5 shows relationship between count and Rayleigh at the zenith with four wavelengths. Note that background counts were subtracted before calculating the relationship, because an individual difference of the background offset level (~20-70 counts) exists. The background offset causes a narrower dynamic range, so we have to choose setting of gain and exposure time for aurora/airglow observations carefully. The relationships between count and Rayleigh with 486, 558, and 630-nm band-pass filters are very close, and that with 428-nm filter has higher ratio of count to Rayleigh. This difference mainly comes from characteristics of the spectral sensitivity of the CCD image sensor of the WMI system. The sensitivity at 428-nm wavelength is about 0.6 times smaller than that at 558-nm wavelength, and the spectral sensitivity has a peak around 600-nm. The relationship between count and Rayleigh is written using the following equations:

$$[\mathrm{Count'}] = 255 \times ([\mathrm{Count}] / 255)^{(1/\gamma)} \quad (3)$$

$$[\mathrm{Rayleigh}] = a \times [\mathrm{Count'}] + b \quad (4)$$

where Count' indicates the "corrected count" using the Gamma correction. We have used the Gamma correction to have a better dynamic range in the dark region, and usually use 0.45 as the Gamma (γ) value. The coefficient values of a and b based on the calibration with four Watec camera and four filters are summarized in Table 2. Each error bar in Figure 5 indicates the standard deviation of counts around the zenith. Basically shorter exposure time of the WMI imager gives a wider dynamic range, but average noise level becomes larger than that with longer exposure time. Table 2 summarizes actual noise level and observable luminosity measured with four wavelengths (428-nm, 486-nm, 558-nm, and 630-nm). The average noise levels in Table 2 were derived from the standard deviation of 9 × 9 pixels around the zenith when the background luminosity was ~600 Rayleigh. We have confirmed that the average noise levels increase due to increase of shot noise when the background luminosity increases. The average noise levels with the 428-nm filter are larger than those with other three filters. Observable luminosity with the 486-nm, 558-nm, and 630-nm filters and a camera setting of the maximum gain (41 dB) was about 40-4000 Rayleigh for 1.07-sec exposure time. When the exposure time is extended to 4.27-sec, the noise level is reduced to about one fourth, but the upper limit of the observable range drops to about 1200 R. Note that available shutter speeds are summarized in Table 1. They are suitable for observations of airglows and weak auroras. On the other hand, the observable luminosity with the 428-nm filter becomes wider than the other three filters. For the purpose of studying of bright auroras such as substorm breakup and auroral arcs, settings of the gain should be changed from the maximum to a lower value (25 dB, for example), because intensity of auroras sometimes exceeds the upper limit. As the H_β emissions (486-nm) typically have an intensity of 100-150 R [e.g., Fujii et al., 2009], the WMI system is potentially capable of detecting the H_β emissions. We have also confirmed that differences of the relationship between count and Rayleigh according to each individual camera are rather small.

For the band-type auroral emissions at the wavelength of ~670-nm, we have used a filter with FWHM of 50 nm. We have also continuously obtained the 670-nm aurora data with the WMI system at several places, to perform quantitative investigation of auroral emissions. Note that the color cameras (WAT-233 and WAT-221S2) to distinguish clouds and auroras have been utilized without any filter.

4. Comparison of WMI 428-nm aurora emission data with high-sensitive EMCCD camera data

Since auroral emission around 428-nm is known as a band emission, a careful quantitative verification is required for the WMI observation with the 428-nm band-pass filters (FWHM of 10-nm). In this study, we investigated whether the WMI system has the estimation capability of the 428 nm auroral emission intensity, by comparing with 428 nm aurora emission data observed simultaneously by the ASI-2 with the narrow band-pass filter.

Figure 6 shows the comparison between 428-nm aurora emission intensities around the zenith measured with a WMI imager and monochromatic EMCCD imager at Tromsø between 23 and 24 UT on 14 March 2015. Both imagers utilized 428-nm band-pass filters, but FWHM of the filter for the EMCCD imager was about 2 nm. Exposure time of the WMI and EMCCD imagers were 4.27 sec and 2.00 sec, respectively. As shown in Figure 6, both 428-nm auroral intensities were almost identical throughout the 1-h interval, except for relatively brighter auroral intensities around 23:16 UT and 23:18 UT during which the poleward expanding and intensifying aurora was measured after substorm onset. The WMI imager data were saturated around 23:16 UT, while the WMI auroral intensity around 23:18 UT is weaker than the EMCCD one. This result suggests that, the WMI imager is practically impossible to detect 428-nm auroral emission intensities properly during brighter aurorae or the WMI data must be considered with caution for quantitative investigation of the brighter 428-nm auroral variations (> 1800 R). Nevertheless, the WMI imager data are very useful because they are in a fairly good agreement with the EMCCD imager data at least for < 1800 R. We can utilize the WMI system for brighter auroras (> 1800 R) if we change settings of the WMI camera (i.e., shorter exposure time and/or lower gain).

5. Locations and acquired data of the WMI imagers

Figure 7 shows locations of the WMI system with FOV coverages projected to 110 km and 250 km altitudes. Their locations are summarized in Table 3. Distribution of the WMI imagers in northern Scandinavia is rather dense, in

244 the horizontal range of about 50-500 km. The distribution of multipoint sites is suitable for research on three-
245 dimensional structures of auroras using the auroral tomography method [e.g., Aso et al., 1998; Tanaka et al., 2011].
246 428-nm and 558-nm monochromatic aurora data obtained at the multipoint sites will be newly used for the
247 mesoscale auroral research, in combination with the current European incoherent scatter (EISCAT) radars and
248 future EISCAT_3D radar system [e.g., McCrea et al., 2015; Tsuda et al., 2017]. Figure 8 shows examples of auroral
249 images taken by the WMI system, and a result of aurora computed tomography analysis by using the WMI auroral
250 images taken at Skibotn, Kilpisjarvi, and Tjautjas at 18:12:21 UT on February 19, 2018. The tomography result
251 shows height variations of the 558-nm auroral arc along geographic longitude (See Figure 8b). Intensity of the
252 auroral arc peaks at an altitude of about 115 km and extends to an altitude of about 140 km. On the other hand,
253 multipoint observations of 630 nm emission in the horizontal range of about a few 1000 km are useful for studies
254 on large scale phenomena such as dynamic variation of auroral oval and drift motion of polar patches.
255 Longyearbyen in Svalbard, South Pole and McMurdo stations are often located in the polar cap region, so their
256 630 nm emission data have been used for research on the polar patches. The WMI system will be also used for
257 study on geomagnetically conjugate auroras in the auroral zone, polar cap, and sub-auroral regions.
258
259 Table 4 summarizes the status of WMI observations at each site. We started monochromatic imager observations
260 in Tromsø and Longyearbyen in 2013, and have been extended the observations in northern Scandinavia and
261 Antarctica. The camera data have been complementarily used with a collocated high sensitivity EMCCD all-sky
262 camera system at each site. Typical exposure time we used is 4-sec for 428-nm emission, 1-sec for 558-nm
263 emission, and 4-sec for 630-nm emission. They are faster than those of the all-sky imager (ASI) that has been
264 operated at the South Pole Station [Ebihara et al., 2007], for example. The 630-nm emission data are used not only
265 for auroral study, but also airglow observation such as polar patches in the polar cap region. Panchromatic and
266 color all-sky camera observations have been also continuously conducted for dayside auroral pulsation study [e.g.,
267 Motoba et al., 2017] even during new moon periods, as well as narrow/wide FOV camera observations mentioned
268 in the previous section. At the South Pole and McMurdo stations, all the cameras can be operated for 24 hours a
269 day between April and August.
270

In the future, similar WMI systems will be installed in Sanae (South Africa), Maitri (India), and Princess Elisabeth (Belgium) stations in Antarctica under international collaborations. The installation realizes a wide area coverage of auroral/airglow observations and is expected to contribute to the quantitative understanding of aurora physics including interhemispheric auroral research [e.g., Motoba et al., 2012]. Most of the data obtained by the multipoint observations with the WMI system will be converted into CDF format files under the IUGONET project, and they can be handled in a unified manner with software packages provided by the SPEDAS project.

5. Summary

This paper has indicated that the WMI observation – which utilizes an inexpensive imager system equipped with a sensitive Watec camera, a filter with high transmittance, and the optics which does not make a parallel ray path – is effective for research on auroras and atmospheric airglows. Cost of the WMI system is roughly two orders lower than those of monochrome imagers conventionally used for aurora/airglow studies. Compared to conventional imager systems, installation of the WMI system in multiple places is easier, and the risk of the WMI camera damage due to twilight or moonlight is relatively low. It is therefore expected that an increase of the number of the WMI cameras realizes observations with various settings according to the required wavelength and necessary observable luminosity range, and wide-area coverage by multipoint observations. In particular, it is important to obtain (1) 428-nm auroral data at multipoint sites (located in the horizontal range of about 50-100 km) for research on three-dimensional structure of auroras using the auroral tomography method, and (2) multipoint observations with a wavelength of 630-nm (in the horizontal range of about a few 1000 km) for study of large scale phenomena such as dynamic variation of the auroral oval and drift motion of polar patches. It is also expected that the system will be effectively utilized for the study of airglow in mid- and low latitude ionosphere (for examples, observations of the atmospheric gravity wave and plasma bubble in the equatorial region). Thus the WMI system is expected to be further developed and spread to the global-scale upper atmospheric observations of multi-wavelength auroras and airglows. Most of the current WMI databases are open to the public via the web page (http://pc115.seg20.nipr.ac.jp/www/opt/index.html).

298

299

300

Data Availability:

Datasets related to this article can be found at http://pc115.seg20.nipr.ac.jp/www/opt/index.html.

Acknowledgments:

We thank I. Sugita and Y. Kadowaki of the National Institute of Polar Research (NIPR), for their helpful support of the MWI data management and calibration. This research was financially supported by the Grants-in-Aid for Scientific Research S (15H05747), Scientific Research B (17H02968) and Scientific Research C (17K05672) by the Ministry of Education, Science, Sports and Culture, Japan. This work was also supported by ROIS-DS-JOINT (001RP2018, and 019RP2018). The WMI system was calibrated at the calibration facility of NIPR, Japan. The production of this paper was supported by a NIPR publication subsidy. This work was partially carried out at the joint research workshop of the Institute for Space-Earth Environmental Research (ISEE), Nagoya University.

References:

Akasofu S-I., The development of the auroral substorm. Planet. Space Sci., Vol. 12 (1964), pp 273-282.

Angelopoulos, V., P. Cruce, A. Drozdov, E. W. Grimes, N. Hatzigeorgiu, D. A. King, D. Larson, J. W. Lewis, J. M. McTiernan, D. A. Roberts, C. L. Russell, T. Hori, Y. Kasahara, A. Kumamoto, A. Matsuoka, Y. Miyashita, Y. Miyoshi, I. Shinohara, M. Teramoto, J. B. Faden, A. J. Halford, M. McCarthy, R. M. Millan, J. G. Sample, D. M. Smith, L. A. Woodger, A. Masson, A. A. Narock, K. Asamura, T. F. Chang, C.-Y. Chiang, Y. Kazama, K. Keika, S. Matsuda, T. Segawa, K. Seki, M. Shoji, S. W. Y. Tam, N. Umemura, B.-J. Wang, S.-Y. Wang, R. Redmon, J. V. Rodriguez, H. J. Singer, J. Vandegriff, S. Abe, M. Nose, A. Shinbori, Y.-M. Tanaka, S. UeNo, L. Andersson, P. Dunn, C. Fowler, J. S. Halekas, T. Hara, Y. Harada, C. O. Lee, R. Lillis, D. L. Mitchell, M. R. Argall, K. Bromund, J. L. Burch, I. J. Cohen, M. Galloy, B. Giles, A. N. Jaynes, O. Le Contel, M. Oka, T. D. Phan, B. M. Walsh, J. Westlake, F. D. Wilder, S. D. Bale, R. Livi, M. Pulupa, P. Whittlesey, A. DeWolfe, B. Harter, E. Lucas, U. Auster, J. W. Bonnell, C. M. Cully, E. Donovan, R. E. Ergun, H. U. Frey, B. Jackel, A.

328 Keiling, H. Korth, J. P. McFadden, Y. Nishimura, F. Plaschke, P. Robert, D. L. Turner, J. M. Weygand, R. M.
329 Candey, R. C. Johnson, T. Kovalick, M. H. Liu, R. E. McGuire, A. Breneman, K. Kersten, P. Schroeder (2018),
330 The Space Physics Environment Data Analysis System (SPEDAS), Space Sci. Rev., 215:9,
331 https://doi.org/10.1007/s11214-018-0576-4.
332 Aso, T., Ejiri, M., Urashima, A., Miayoka, H., Steen, A., Brandstrom, U., and Gustavsson, B. (1998), First results
333 of auroral tomography from ALIS-Japan multi-station observations in March, 1995, Earth Planets Space, 50,
334 81–86.
335 Donovan, E.F., S. Mende, B. Jackel, H. Frey, M. Syrjäsuo, I. Voronkov, T. Trondsen, L. Peticolas, V. Angelopoulos,
336 S. Harris, M. Greffen, M. Connors (2006), The THEMIS all-sky imaging array—system design and initial
337 results from the prototype imager. J. Atmos. Terr. Phys. 68, 1472–1487.
338 Ebihara, Y., Y.-M. Tanaka, S. Takasaki, A. T. Weatherwax, and M. Taguchi (2007), Quasi-stationary auroral
339 patches observed at the South Pole Station, J. Geophys. Res., 112, A01201, doi:10.1029/2006JA012087.
340 Fujii, R., Y. Iwata, S. Oyama, S. Nozawa, and Y. Ogawa (2009), Relations between proton auroras, intense electric
341 field, and ionospheric electron density depletion, J. Geophys. Res., VOL. 114, A09304,
342 doi:10.1029/2009JA014319.
343 Hayashi, H., Y. Koyama, T. Hori, Y. Tanaka, S. Abe, A. Shinbori, M. Kagitani, T. Kouno, D. Yoshida, S. UeNo, N.
344 Kaneda, M. Yoneda, N. Umemura, H. Tadokoro, T. Motoba and IUGONET project team (2013), Inter-
345 university Upper Atmosphere Global Observation NETwork (IUGONET), Data Sci. J., 12, WDS179-WDS184,
346 doi: 10.2481/dsj.WDS-030.
347 Kataoka, R., Y. Miyoshi, T. Sakanoi, A. Yaegashi, Y. Ebihara, and K. Shiokawa (2011), Ground-based
348 multispectral high-speed imaging of flickering aurora, Geophys. Res. Lett., Vol. 38 (14).
349 McCrea, I. W., A. Aikio, L. Alfonsi, E. Belova, S. Buchert, M. Clilverd, N. Engler, B. Gustavsson, C. Heinselman,
350 J. Kero, M. Kosch, H. Lamy, T. Leyser, Y. Ogawa, K. Oksavik, A. Pellinen-Wannberg, F. Pitout, M. Rapp, I.
351 Stanislawska, and J. Vierninen (2015), The science case for the EISCAT_3D radar, Progress in Earth and
352 Planetary Science, doi:10.1186/s40645-015-0051-8.
353 Motoba, T., K. Hosokawa, A. Kadokura, and N. Sato, Magnetic conjugacy of northern and southern auroral beads,
354 Geophys. Res. Lett., Vol. 39 (2012), L08108, doi:10.1029/2012GL051599.

355 Motoba, T., Ebihara, Y., Kadokura, A., Engebretson, M. J., Lessard, M. R., Weatherwax, A. T., and Gerrard, A. J.
356 (2017), Fast-moving diffuse auroral patches: A new aspect of daytime Pc3 auroral pulsations, *J. Geophys. Res.*
357 *Space Physics*, 122, 1542– 1554, doi:10.1002/2016JA023285.
358 Ogawa, Y., A. Kadokura, T. Motoba, Y. Tanaka, and K. Hosokawa (2013), Processing and visualization of large
359 amounts of auroral data obtained with All-sky/Narrow field-of-view parallel imagers in Tromso and
360 Longyearbyen, Journal of Space Science Informatics Japan, vol. 2, 51-61.
361 Ozaki, M., K. Shiokawa, Y. Miyoshi, K. Hosokawa, S. Oyama, S. Yagitani, Y. Kasahara, H. Kojima, Y. Kasaba, S.
362 Matsuda, R. Kataoka, Y. Ebihara, Y. Ogawa, Y. Otsuka, S. Kurita, R. Moore, Y. Tanaka, M. Nose, T. Nagatsuma,
363 M. Connors, N. Nishitani, Y. Katoh, M. Hikishima, A. Kumamoto, F. Tsuchiya, A. Kadokura, T. Nishiyama, T.
364 Inoue, K. Imamura, A. Matsuoka, and I. Shinohara (2018), Microscopic observations of pulsating aurora
365 associated with chorus element structures: Coordinated Arase satellite: PWING observations, Geophys. Res.
366 Lett., DOI: 10.1029/2018GL079812.
367 Taguchi, M., M. Ejiri, and K. Tomimatsu (2004), A new all-sky optics for aurora and airglow imaging, Adv. Polar
368 Upper Atmos. Res., 18, 140–148.
369 Tanaka, Y.-M., T. Aso, B. Gustavsson, K. Tanabe, Y. Ogawa, A. Kadokura, H. Miyaoka, T. Sergienko, U.
370 Brändström, and I. Sandahl (2011), Feasibility study on Generalized - Aurora Computed Tomography, Ann.
371 Geophys., vol. 29, 551-562.
372 Tanaka, Y., A. Shinbori, T. Hori, Y. Koyama, S. Abe, N. Umemura, Y. Sato, M. Yagi, S. UeNo, Satoru, A. Yatagai,
373 Y. Ogawa, and Y. Miyoshi (2013), Analysis software for upper atmospheric data developed by the IUGONET
374 project and its application to polar science, Advances in Polar Science, doi: 10.3724/SP.J.1085.2013.00231,
375 vol. 24, No. 4, 231-240.
376 Tsuda, T., M. Yamamoto, H. Hashiguchi, K. Shiokawa, Y. Ogawa, S. Nozawa, H. Miyaoka and A. Yoshikawa
377 (2016), A proposal on the study of solar-terrestrial coupling processes with atmospheric radars and ground-
378 based observation network, Radio Science, 51, doi: 10.1002/2016RS006035.
379
380

Figure captions:

Figure 1: Pictures of the WMI imagers in (a) Tromsø and (b) Longyearbyen. The system includes several all-sky cameras with filters of different wavelengths, and also narrow field of view (FOV) and/or wide FOV camera(s). (c) Schematic illustration of the WMI imager with the Fujinon's fish-eye lens, Watec camera, and the Techspec's band-pass filter.

Figure 2: An overview of the WMI system. It consists of (a) the imager system at observation sites and (b) the data servers in the National Institute of polar research (NIPR). Arrows in the figure indicate flows of image data.

Figure 3: Transmittances of three filters with wavelengths of (a) 428-nm, (b) 558-nm, and (c) 630-nm. Each line indicates different incident angles between 0 and 20 degrees. Three vertical lines indicate the locations of auroral emissions at wavelengths of 427.8-nm, 557.7-nm, and 630.0-nm. The symbols marked in the bottom of each plot indicate theoretical changes of the center wavelength of each filter based on equation 1.

Figure 4: Examples of (a) an original image, (b) the limb darkening characteristics of the WMI imager, and (c) a calibrated image after flat field correction. Background noise level was subtracted before the flat field correction. Note that all the WMI cameras use the settings of a gamma value of 0.45 and the maximum gain value (41 dB).

Figure 5: The relationship between the corrected count and Rayleigh for the WMI system with four different wavelengths (428, 486, 558, and 630-nm) and different exposure times (1.07-sec and 4.27-sec). Note that all the WMI cameras use the settings of a gamma value of 0.45 and the maximum gain value (41 dB).

Figure 6: Comparison of 428-nm emission data between the WMI system (red) and the ASI-2 with EMCCD imager (black), obtained in Tromsø on March 14, 2015. A dashed line indicates the upper limit of WMI observation with the settings of 4.27-sec exposure time, a gamma value of 0.45, and the maximum gain value (41 dB).

Figure 7: Locations of the WMI system, and coverages of observable regions projected into (green) 110 km and (red) 250 km altitudes. The edge of the all-sky circle is at 70 degrees from the zenith.

Figure 8: (Left) Auroral images at a wavelength of 558 nm observed with WMI at 6 locations at 18:12:21 UT on February 19, 2018. Each image is projected into 110 km altitude. (Right) A result of aurora computed tomography analysis by using the WMI auroral images taken at Skibotn, Kilpisjarvi, and Tjautjas at 18:12:21 UT on February 19, 2018. The center position of panels a, b, and c is set at 68.58 deg geographic north and 20.63 deg geographic east, and x and y indicate the local Cartesian coordinates in the zonal and meridional directions.

420

421 Table 1: Product names and their specifications composing the WMI system

422

Camera	Watec WAT-910HX/RC (CCD: Sony ICX428ALL, CCD size: 7.40 mm × 5.95 mm (1/2 inch)) Minimum Illumination 0.0000025 Lux (× 256 frames, F1.4) Shutter speeds used: 0.25, 0.53, 1.07, 2.14, and 4.27 sec (×256 frames)
Lens	Fujinon Fish-eye lens YV2.2x1.4A-SA2 Focus length: 1.4-3.1 mm, F1.4, FOV: 185° × 185°
Optical filter	Techspec, 25 mm diameter, hard coated OD4 10 nm band-pass filter Center wavelengths: 430, 488, 560, and 632 nm FWHM: 10 nm Techspec, 25 mm diameter, hard coated OD4 50 nm band-pass filter Center wavelength: 675 nm FWHM: 50 nm
Video encoder	AXIS Q7404 Image resolution: 640 pixels × 480 pixels, Image format: jpeg (8bit), AXIS Q7424-R Image resolution: 640 pixels × 480 pixels, Image format: jpeg (8bit)

423

424

Table 2: Summary of average noise level and observable luminosity at each wavelength. The observable luminosity was estimated taking subtraction of background (~20-80 counts) and the maximum count (256 counts, 8-bit) into account. All the WMI cameras use the settings of a gamma correction value of 0.45 and the maximum gain value (41 dB). The average noise levels were calculated when the background luminosity was ~600 Rayleigh. The a and b in the table indicate each coefficient of Equation 4.

Aurora/air glow emission	Wavelength of filter	Exposure time	Serial number of camera	a	b	Average noise level	Observable luminosity
428 nm (N_2^+)	430±5 nm	1.07 sec	03632	45.01	99.15	190 R	220-6000 R
		4.27 sec	03632	10.25	30.03	60 R	70-1800 R
486 nm (H_β)	488±5 nm	1.07 sec	03633	20.95	112.83	180 R	230-4000 R
		4.27 sec	03633	5.27	16.68	40 R	40-1200 R
558 nm (OI)	560±5 nm	1.07 sec	03631	21.63	118.85	200 R	200-4000 R
		4.27 sec	03631	5.54	40.95	60 R	90-1200 R
630 nm (OI)	632±5 nm	1.07 sec	02933	22.69	90.92	140 R	200-4000 R
		4.27 sec	02933	5.52	8.92	30 R	20-1200 R

433

434 Table 3: Locations of multi-wavelength WMI observation stations, including possible ones near future (in Italic).

435

Location name	Code	Geographic Latitude (deg)	Geographic longitude (deg)	Geomagnetic latitude (deg)
Longyearbyen	LYR	78.15	16.03	75.16
Tromsø	TRO	69.58	19.22	66.53
Skibotn	SKB	69.35	20.36	66.23
Kilpisjarvi	KIL	69.05	20.78	65.90
Kiruna	KRN	67.84	20.41	64.68
Tjautjas	TJA	67.33	20.75	64.14
Sodankylä	SOD	67.42	26.39	63.96
South pole	SPA	-90.00	139.27	-74.11
McMurdo	MCM	-77.82	166.66	-79.97
Sanae	*SAN*	*-72.67*	*-2.83*	-62.08
Maitri	*MAI*	*-70.77*	*11.73*	-62.83
Princess Elisabeth	*PEA*	*-71.95*	*23.33*	-65.29
Syowa	*SYO*	*-69.19*	*41.05*	-66.69

436

437

Table 4: Wavelength and exposure time used for the WMI system at each station. Each number in the table indicates exposure time of WMI camera data (equivalent to its time resolution). Note that asterisk (*) indicates usage of band-pass filters with wider bandwidth (FWHM of ~100 nm, see Ogawa et al., 2013). “BW” indicates panchromatic black-white image data, and “Color” indicates color image data taken with WAT-233 (with 4-sec exposure time) and WAT-221S2 (with 1-sec exposure time).

Site	Start	End	428nm	558nm	630nm	670nm	BW	Color
TRO	2011-01	2013-03	1*	1*	1*	-	1	-
	2013-10	2014-03	-	1	4	1	0.5	-
	2014-09	2016-03	4	1	4	1	0.25	4
	2016-09	2019-03	-	1	4	0.5	-	1
LYR	2011-01	2013-03	1*	1*	1*	-	1	-
	2013-10	2014-03	-	1	4	0.5	0.5	-
	2014-09	2016-03	4	1	4	0.5	0.25	4
	2016-09	2019-03	4	1	4	0.5	0.25	1
SPA	2014-04	2014-08	-	0.5	4	-	0.5	-
	2015-03	2015-08	4	1	4	1	0.5	4
	2016-03	2018-08	-	1	4	1	0.5	-
MCM	2015-03	2018-08	-	4	4	1	-	4
KIL	2016-10	2017-03	4	-	-	-	-	-
	2017-03	2017-04	4	1	-	0.5	-	-
	2017-10	2018-03	4	1	-	0.5	-	1
	2018-10	2019-03	2	1	-	0.5	-	1
KRN	2017-01	2019-03	4	1	-	0.5	-	1
TJA	2017-01	2019-03	4	1	-	0.5	-	1
SKB	2018-02	2018-03	2	1	-	-	-	1

	2018-09	2019-03	1	1	1	-	0.5	1
SOD	2016-09	2019-03	-	1	-	-	-	1

445

446

Fig 1


(a)
Narrow FOV
All-sky
Wide FOV
All-sky
All-sky
All-sky
All-sky
All-sky

(b)


All-sky
Narrow FOV
All-sky
All-sky
All-sky
All-sky
All-sky
All-sky

(c)

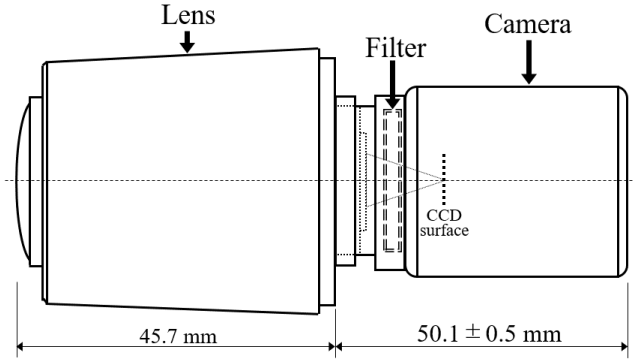
Lens
Filter
Camera
CCD surface
45.7 mm
50.1 ± 0.5 mm

Fig 2

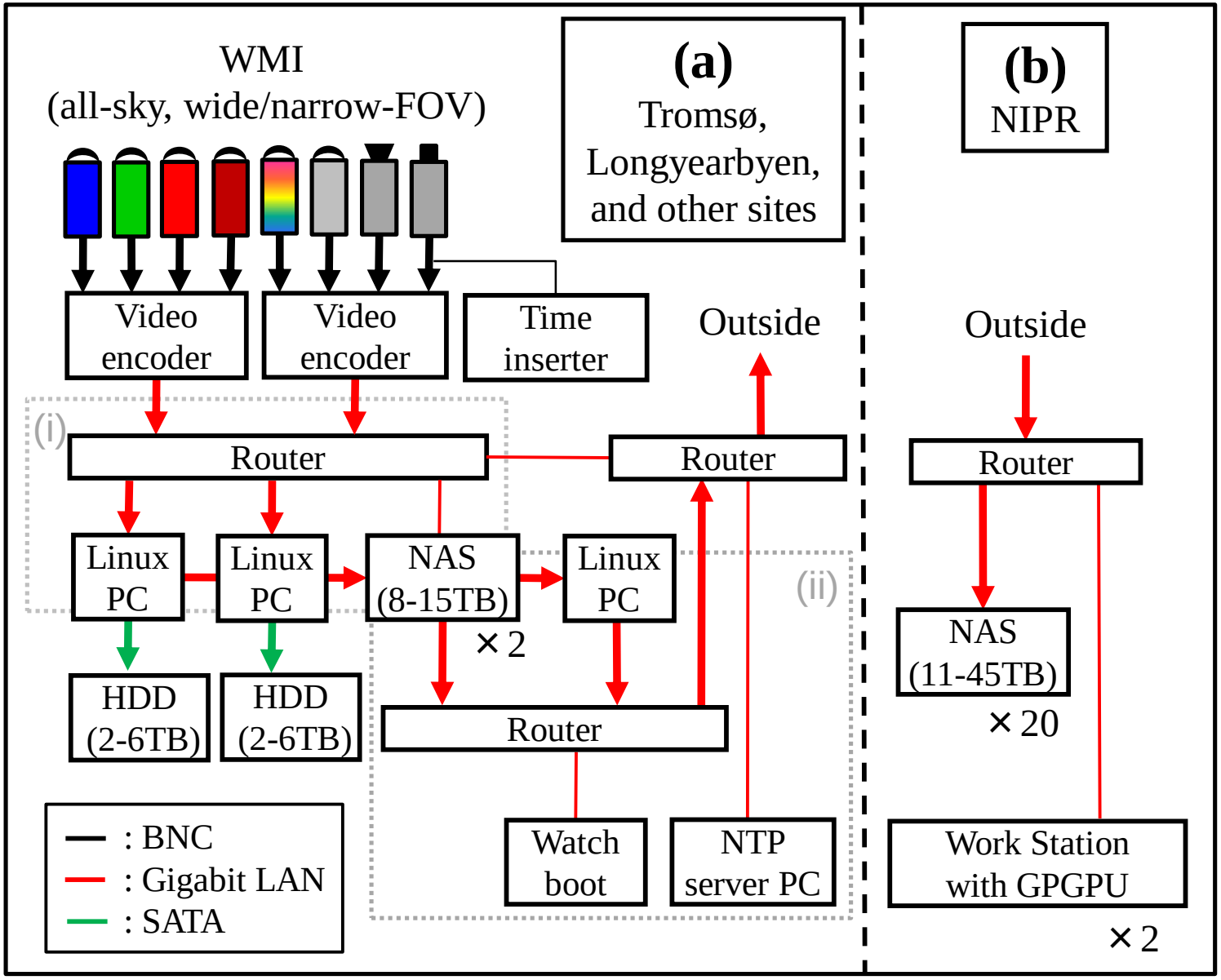
WMI
(all-sky, wide/narrow-FOV)
(a)
Tromsø,
Longyearbyen,
and other sites
(b)
NIPR
Video encoder
Video encoder
Time inserter
Outside
Outside
(i)
Router
Router
Router
Linux PC
Linux PC
NAS (8-15TB)
× 2
Linux PC
(ii)
HDD (2-6TB)
HDD (2-6TB)
Router
NAS (11-45TB)
× 20
Watch boot
NTP server PC
Work Station with GPGPU
× 2
: BNC
: Gigabit LAN
: SATA

Fig 3

(a) 428 nm

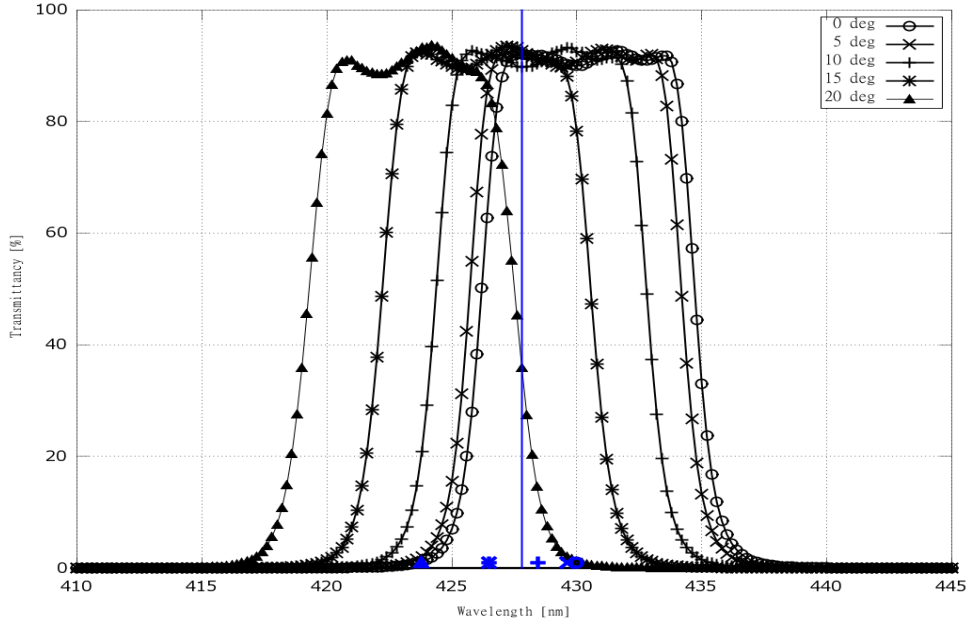

(b) 558 nm

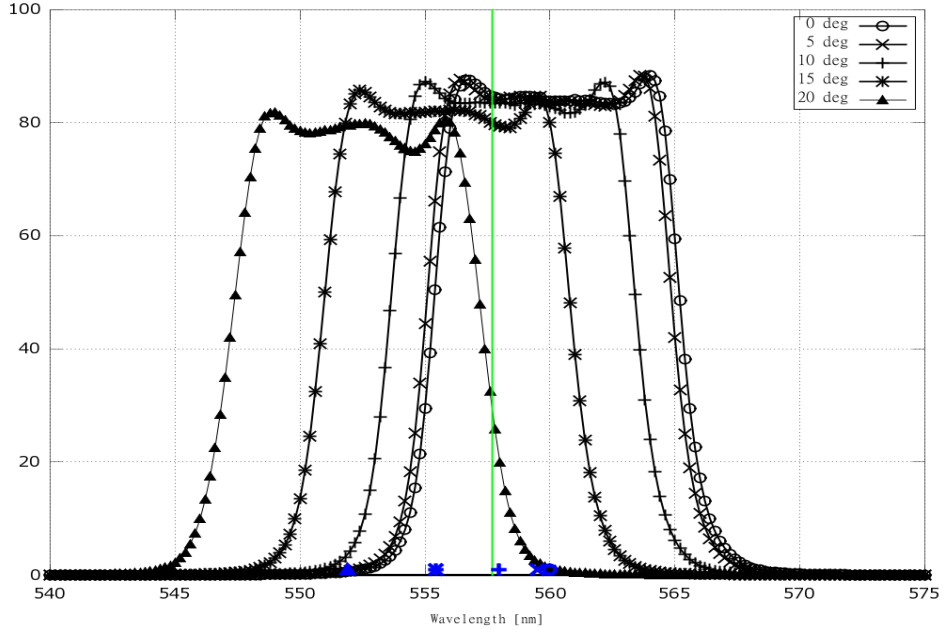

(c) 630 nm

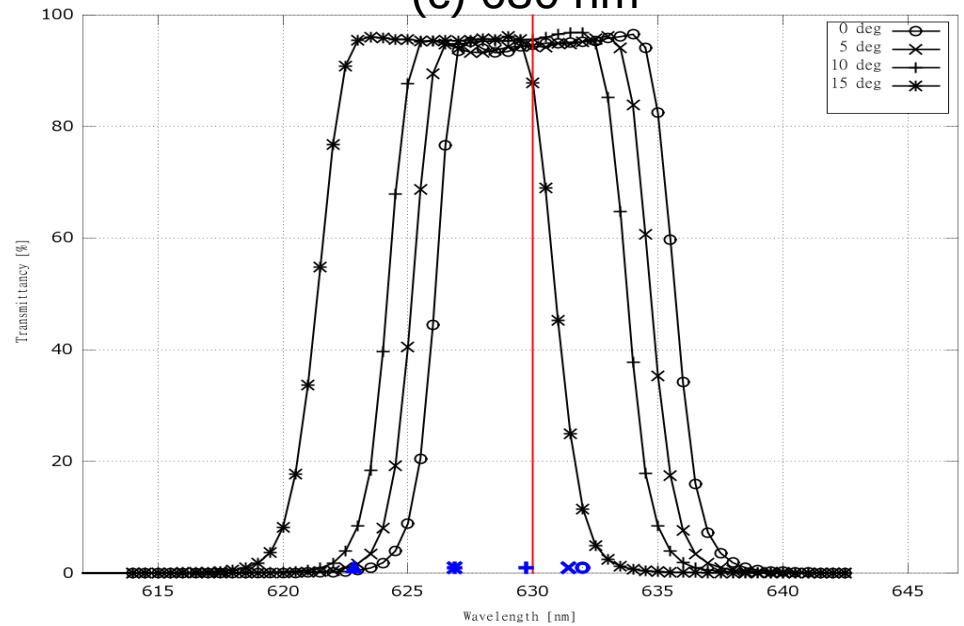

Fig 4

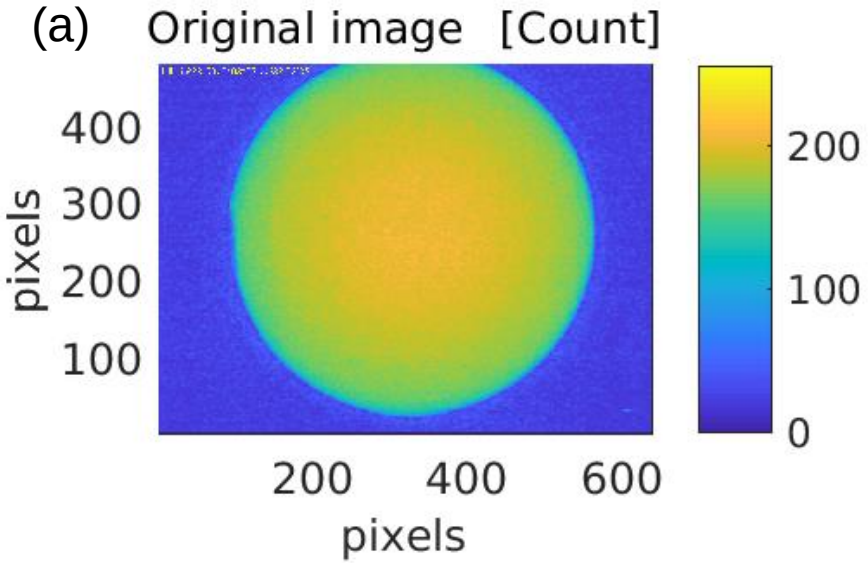

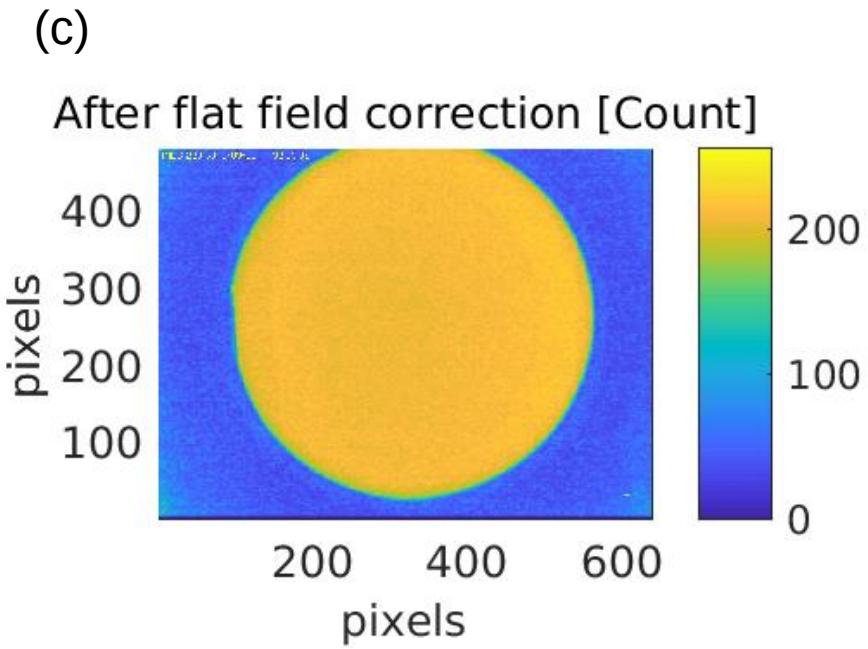

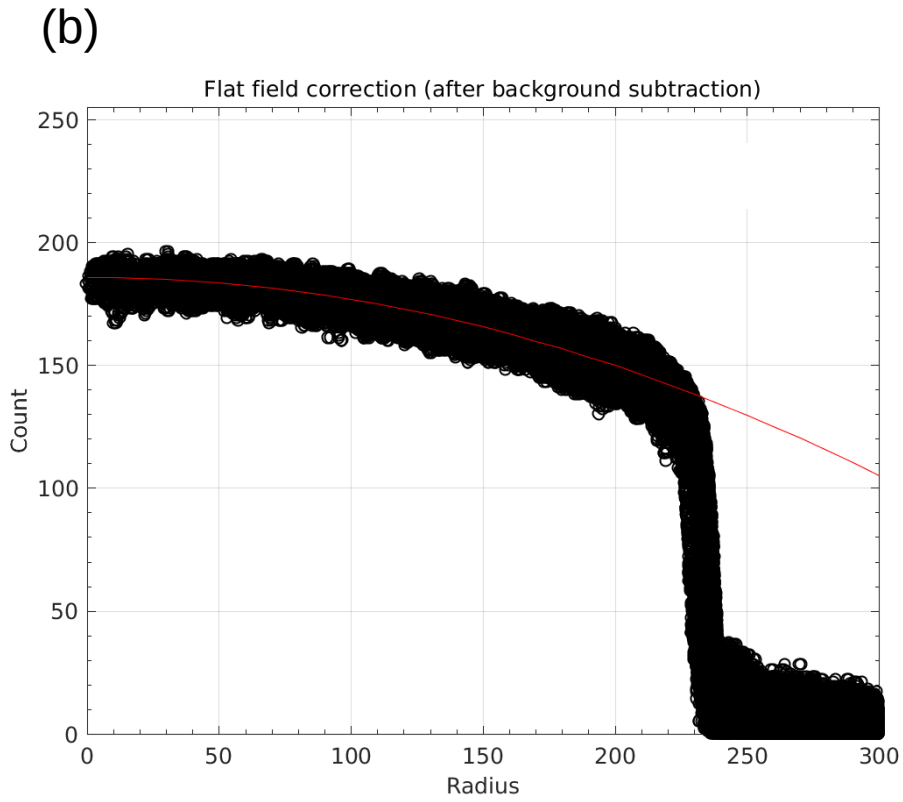

558nm, 1sec

Fig 5

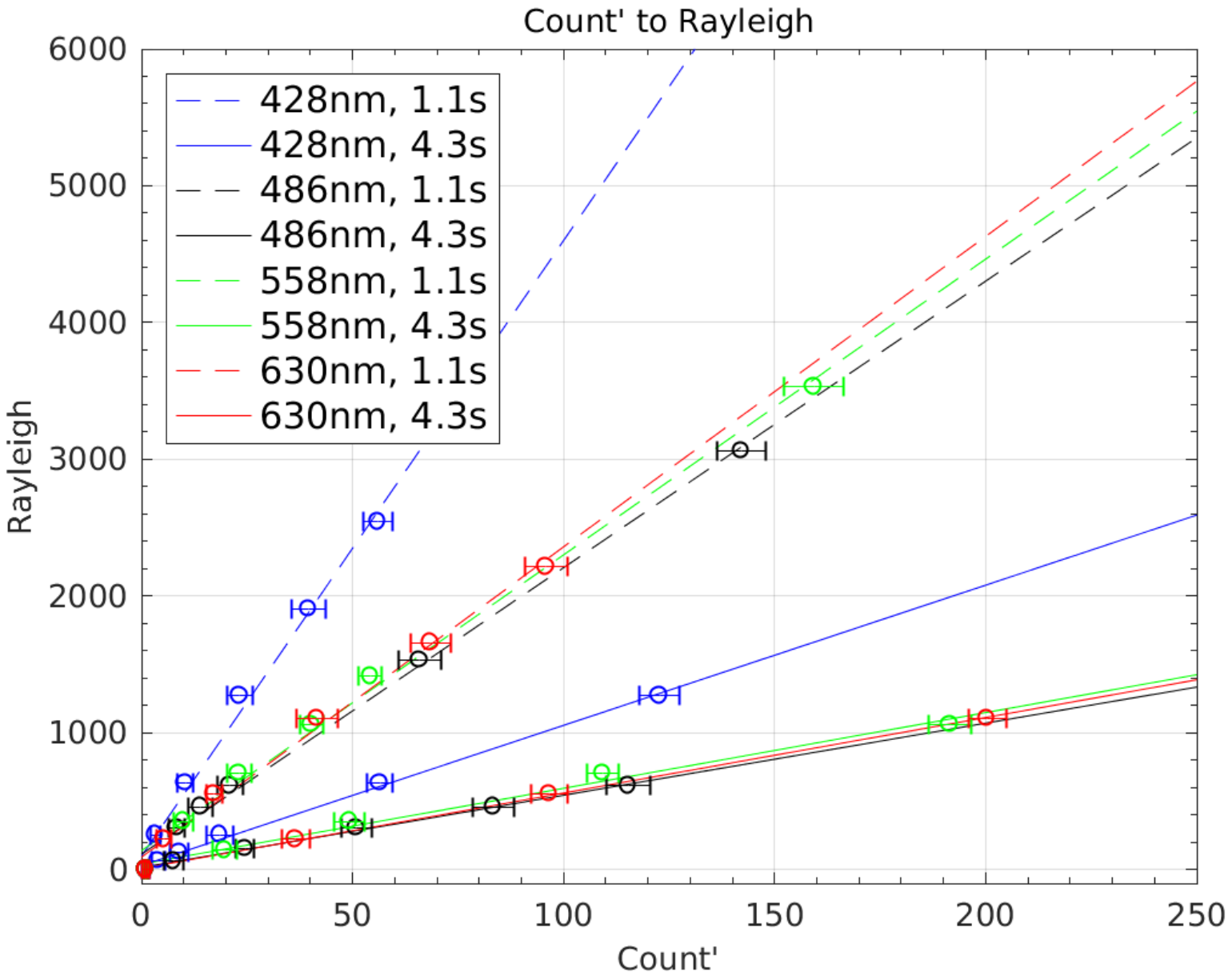
Count' to Rayleigh
428nm, 1.1s
428nm, 4.3s
486nm, 1.1s
486nm, 4.3s
558nm, 1.1s
558nm, 4.3s
630nm, 1.1s
630nm, 4.3s
Rayleigh
Count'
0
1000
2000
3000
4000
5000
6000
0
50
100
150
200
250

Fig 6

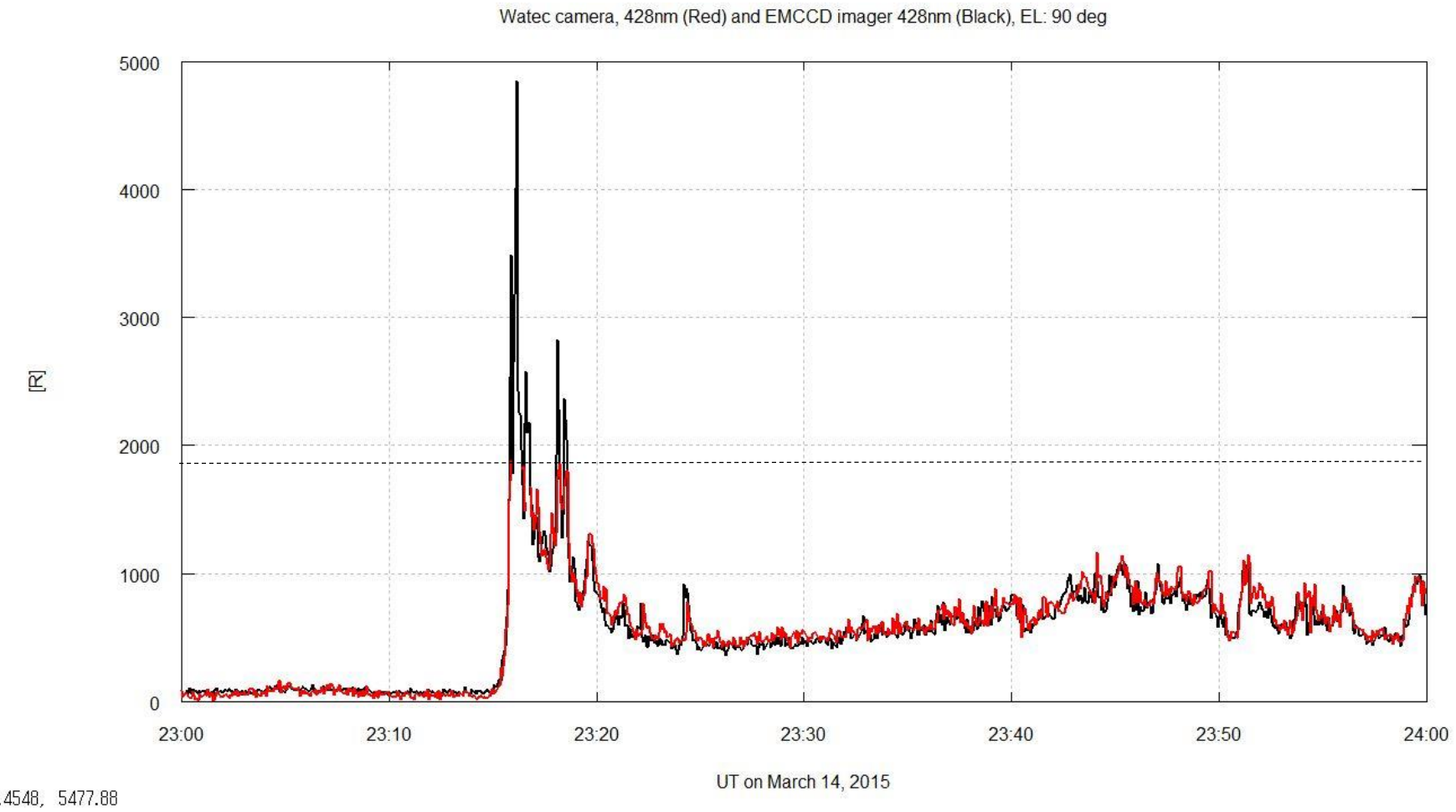

23.4548, 5477.88

Fig 7

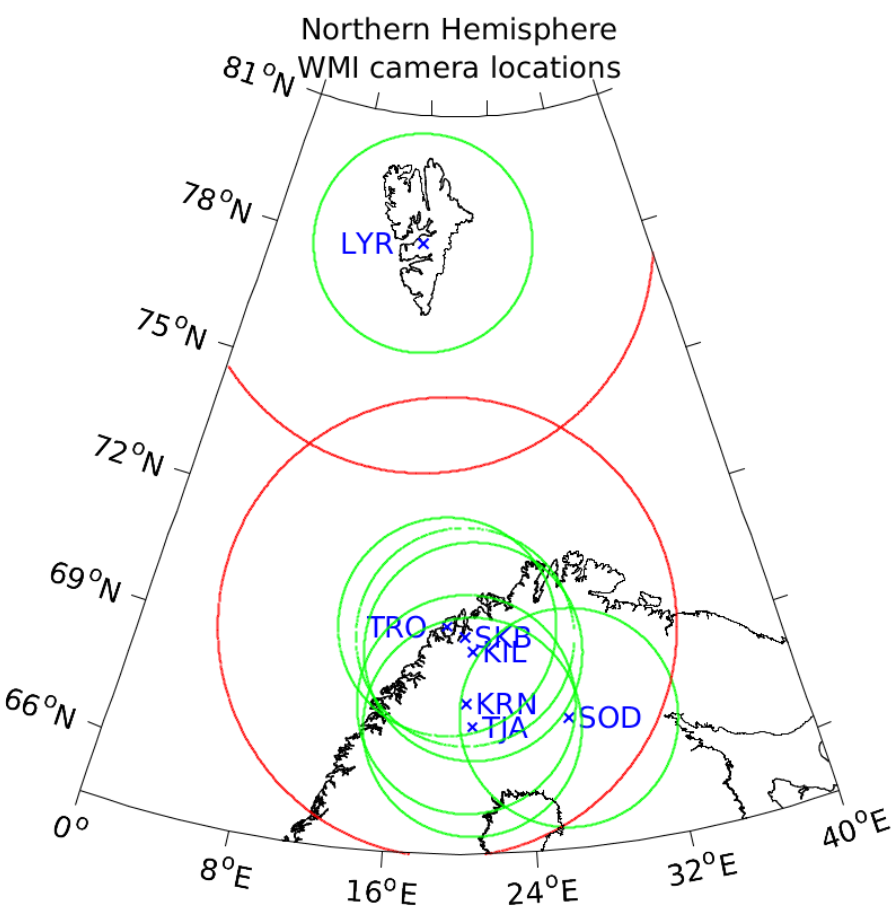
Northern Hemisphere
WMI camera locations
81°N
78°N
75°N
72°N
69°N
66°N
0°
8°E
16°E
24°E
32°E
40°E
LYR
TRO
SKB
KIL
KRN
TJA
SOD

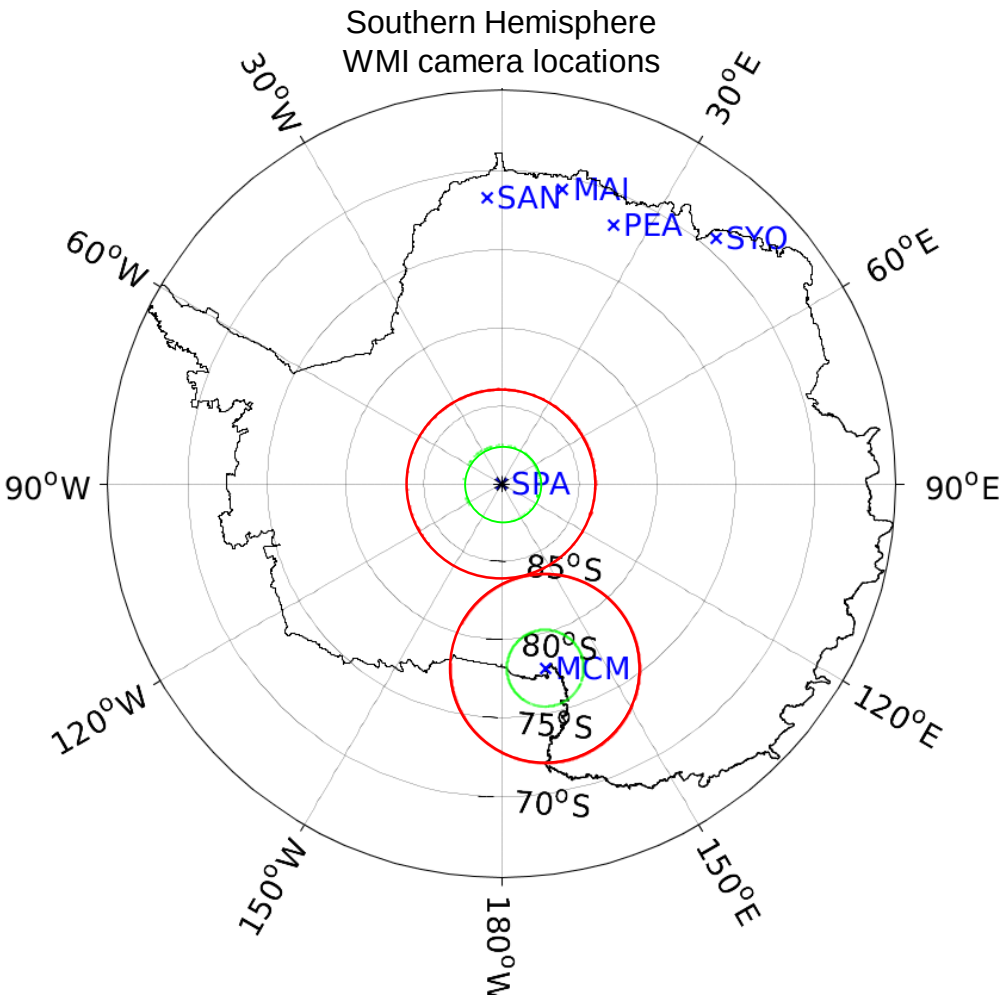
Southern Hemisphere
WMI camera locations
30°W
30°E
60°W
60°E
90°W
90°E
120°W
120°E
150°W
150°E
180°W
SAN
MAI
PEA
SYO
SPA
85°S
80°S
MCM
75°S
70°S

Fig 8

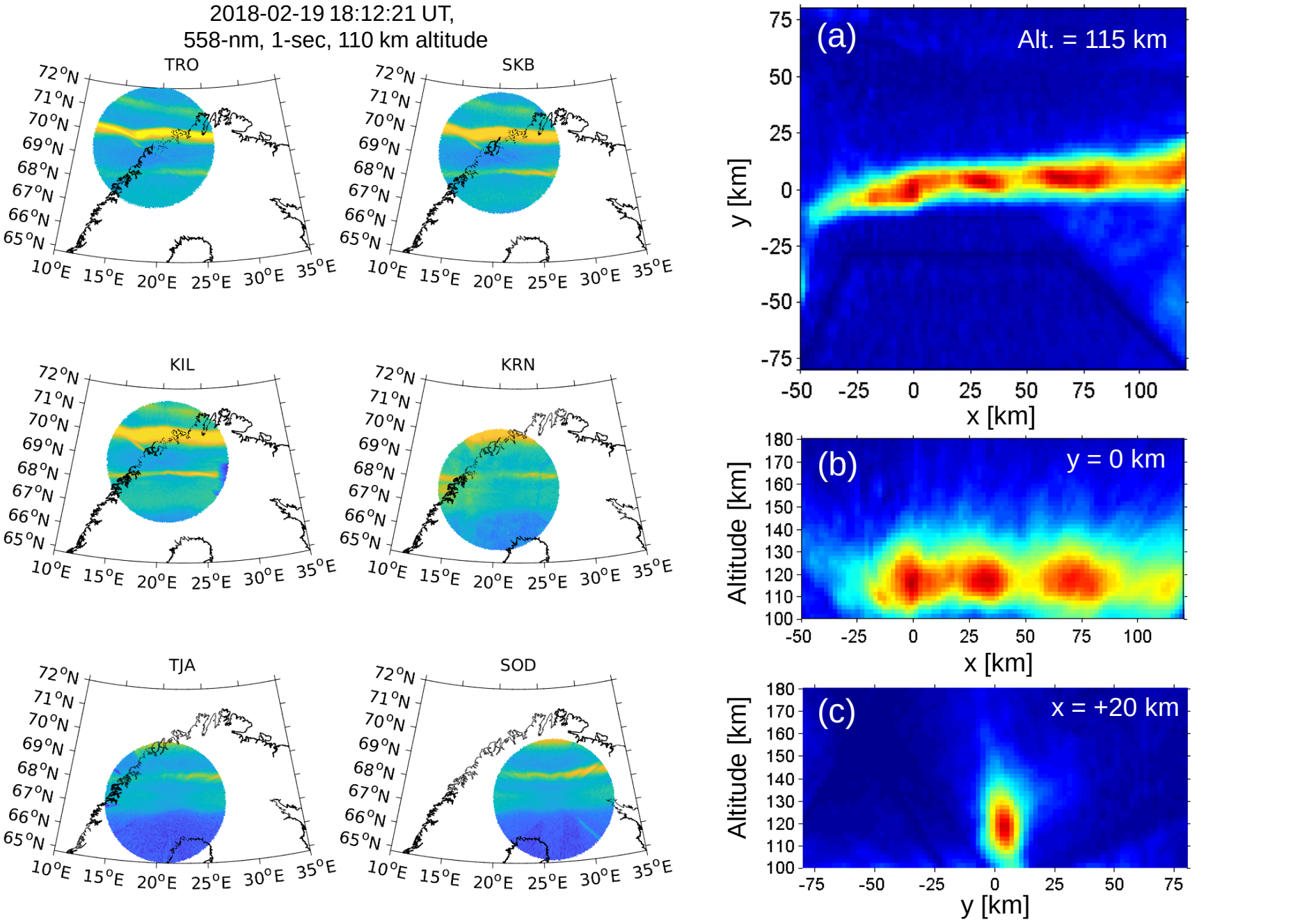
2018-02-19 18:12:21 UT,
558-nm, 1-sec, 110 km altitude
TRO
SKB
KIL
KRN
TJA
SOD
72°N
71°N
70°N
69°N
68°N
67°N
66°N
65°N
10°E
15°E
20°E
25°E
30°E
35°E
(a)
Alt. = 115 km
y [km]
x [km]
(b)
y = 0 km
Altitude [km]
(c)
x = +20 km